IEEE Access
Multidisciplinary | Rapid Review | Open Access Journal

Received 17 April 2024, accepted 23 June 2024, date of publication 3 July 2024, date of current version 15 July 2024.

Digital Object Identifier 10.1109/ACCESS.2024.3422429

RESEARCH ARTICLE

Effective Suppression of Mover-Position-Dependent Resonances Using Combined Decoupled Persistent Oscillation Compensator and Disturbance Observer Structure

YOUNG-SEOK KIM[1], TAE-HO OH[1], DAE-YOUNG YANG[1], SANG-HOON LEE[2], (Member, IEEE), AND DONG-IL CHO[1,2], (Member, IEEE)

[1]Department of Electrical and Computer Engineering and Engineering Institute of Engineering Research, Seoul National University, Seoul 08826, South Korea
[2]Research and Development Center, RS Automation Company Ltd., Pyeongtaek 17709, South Korea

Corresponding author: Dong-Il Cho (dicho@snu.ac.kr)

This work was supported in part by the Technology Development Program of the Ministry of SMEs and Startups (MSS), South Korea, under Grant 00266705; and in part by the Institute of Engineering Research at Seoul National University.

ABSTRACT This paper presents a novel resonance suppression method for mover-position-dependent resonance. In industrial equipment and robots, increasing controller bandwidth for higher performance can induce inherent resonances. Various filter-based methods have been developed and utilized to compensate for the resonances. However, in applications, such as the belt-drive loads, where the resonance frequency can change by two to three times depending on the position of the mover, suppressing the resonance using fixed-parameter filters is not effective. This paper proposes a new resonance suppression method combining a decoupled persistent oscillation compensator (DPOC) and a disturbance observer (DOB). In the proposed method, the DPOC compensates for the mover-position-dependent resonance by attenuating the magnitude of the measured velocity signal within a specific frequency range, whereas the DOB compensates for external disturbances. Therefore, the control system with the proposed method can enhance control performance by automatically adapting to both resonance characteristics dependent on the mover position and the external disturbances. The implementation of the proposed method in the discrete-time domain is also presented, and its stability and robustness are analyzed. Experiments are performed on an industrial belt-drive servo system to demonstrate the effectiveness of the proposed method. Using the proposed method leads to an 84% reduction in overshoot and a 20% reduction in tack time compared with the results of using a well-tuned set of fixed-parameter filters, demonstrating its superiority in resonance suppression.

INDEX TERMS Discrete-time systems, notch filters, resonance suppression, sliding mode control, servosystems.

I. INTRODUCTION

In industrial equipment and robots, high-precision and high-speed control performances are essential requirements. To achieve these objectives, it is necessary to increase the control bandwidth; however, this can amplify high-frequency noise or induce inherent resonances in the system. Such resonances can lead to annoying noise for operators, reduced productivity owing to increased tack time, and physical damage to machinery. Therefore, detecting the presence of resonance, estimating the resonance frequency, and suppressing the resonance are very important topics. This paper focuses on methods for suppressing resonances, particularly in loads where resonance characteristics continuously change

The associate editor coordinating the review of this manuscript and approving it for publication was Zheng Chen.

with the position of the mover, which in turn makes estimating the resonant frequency difficult.

Research on filter-based resonance suppression methods, such as low-pass filters (LPFs) and notch filters (NFs), has become popular for their straightforward design and ease of implementation. Especially, NFs are widely utilized for their precise ability to diminish signals within a narrow frequency band around the notch frequency while allowing other signals to pass through. These characteristics have led to the successful implementation of NFs across a wide range of industrial areas such as wafer scanners [1], biomedical devices [2], power systems [3], and industrial servo systems [4], [5]. NF parameters can be set using the frequency response of the system such as frequency response function (FRF) measurements and fast Fourier transform (FFT) of the current signal or velocity feedback [6], [7], [8]. In particular, FRF measurements have led to research on optimal NF parameter tuning algorithms using multiple FRFs and reinforcement learning because of their rich information [8]. Several researches have been conducted to estimate the frequencies of resonances included in current data to configure the NF parameters in real-time [9], [10], [11]. An adaptive notch filter (ANF), which sets the notch frequency to the estimated resonant frequency by the frequency estimator, has been proposed and successfully applied in industrial servo systems to suppress resonances [10], [12]. The above-mentioned filter-based resonance suppression methods can effectively suppress resonances when there is minimal variation in resonance characteristics depending on the mover position. These resonance characteristics primarily appear in the high-frequency range, typically above 1,000 Hz. However, when resonance characteristics continuously vary with the mover position, it becomes challenging to suppress resonances using fixed-parameter filter-based resonance suppression methods. These resonance characteristics typically occur in situations where the physical characteristics of the load significantly vary with the mover position, such as belt tension in belt-drive loads. These resonance characteristics primarily appear in the mid-frequency range between 100 Hz to 500 Hz. In these cases, skilled experts typically address the situation by progressively adding NFs, sometimes up to five, within the frequency bands where resonances are anticipated. They continue this incremental approach until the resonances are eliminated. However, using too many NFs can decrease the stability of the system because an NF fundamentally induces a phase lag in the frequency range lower than the notch frequency. Therefore, the filter-based resonance suppression methods have limitations in effectively suppressing resonances that continuously vary with the mover position. In the remainder of this paper, we refer to these mover-position-dependent resonance characteristics as a persistent oscillation (PO).

In addition to filter-based resonance suppression methods, various control structures suitable for PO suppression have been developed. The DOB was originally designed to estimate and compensate for external disturbances [13], and research has actively explored modifying the DOB structure or tuning the Q-filter for resonance suppression [14], [15], [16], [17]. In particular, Q-filter design methods for resonance suppression have been actively researched [18], [19]. Recently, a Q-filter design method was developed where the frequency response of the plant is used to establish the plant model, and a suitable Q-filter for the plant model is designed to suppress resonances [18]. In [19], the magnitude of the Q-filter was enhanced in specific frequency bands to better estimate and compensate for resonances. However, these methods require accurate system models. Furthermore, designing an incorrect Q-filter leads to an increase in high-frequency noise. Meanwhile, enhancing the damping parameter of the system is also applicable for suppressing PO. The velocity feedback structure is a prominent example among these methods [20], [21], [22]. The difference between the measured velocity and the velocity under nominal plant conditions is converted into a current unit and fed back to compensate for resonances [20]. The difference between the estimated velocity from the state observer and the velocity under nominal plant conditions is fed back to compensate for the resonances [21], [22]. However, these methods do not provide clear guidance on parameter settings. Recently, research has focused on developing resonance suppression methods involving neural networks [23], [24], [25], adaptive control [26], [27] and iterative control [28], [29]. However, these approaches face challenges to implement in industrial applications for which they require tuning numerous parameters, implementation of complex control structures, and substantial computational resources.

To overcome the limitations of previous studies, this paper introduces a new resonance suppression method for PO. Overall, the main results of this paper are summarized as follows:

1) A new resonance suppression method that combines the DPOC and the DOB is introduced. The DPOC is composed of three main stages: the ideal plant output calculation stage, the PO calculation stage and the filtering stage. The signal processed through these three stages allows the attenuation of the magnitude of the velocity signal in specific frequency bands to suppress PO. Also, the DOB can handle external disturbances, thereby enhancing the control system performance by simultaneously compensating for both PO and external disturbances.
2) To implement the proposed method in the discrete-time domain, a decoupled disturbance compensator (DDC) is utilized instead of the traditional DOB. The DDC is a special type of discrete-time DOB in which the sliding mode dynamics and the disturbance estimation error dynamics are decoupled [30], [31]. Furthermore, the stability and robustness of the system using the proposed method are analyzed.
3) Experiments are conducted on a belt-drive servo system. FRF measurements are obtained by changing the position of the mover in the belt drive system, which

shows that the resonance characteristics continuously vary depending on the mover position. The proposed method is compared with the resonance suppression method using the ANF [10] to demonstrate the effectiveness of the proposed method in PO suppression.

The rest of this paper is organized as follows. Section II discusses the modeling of resonance in different frequency bands and the challenges in suppressing PO. Section III details the effects and design methods of the combined DPOC and DOB structure. Section IV discusses the implementation of the proposed method in the discrete-time domain and its stability and robustness. Section V presents the results of experiments conducted on the industrial belt-drive servo system to demonstrate the effectiveness of the proposed method in PO suppression. Finally, Section VI briefly summarizes the conclusions and future research directions.

II. MODELING OF RESONANCES

The causes of resonance and noise that can occur in industrial equipment and robots can be broadly categorized into three frequency bands: external disturbances in the low-frequency range, noise in the high-frequency range, and unmodeled higher-order dynamics. Figure 1 shows a block diagram of a control system including resonance models. $C(s)$ is the controller, and $H(s)$ are the filters such as LPF and NF. $\theta^{\mathrm{ref}}(s)$ is the position reference, $\theta(s)$ is the measured position (position feedback), $f^{\mathrm{ext}}(s)$ is the external disturbances, and $n(s)$ is the noise from the sensor. The transfer function of the plant model is given by:

$$P(s) = P_n(s)\,\Delta(s) = \frac{k_t}{J_n s^2} \cdot \prod_i \frac{J_{n,i}s^2 + B_{n,i}s + K_{n,i}}{J_{d,i}s^2 + B_{d,i}s + K_{d,i}} \quad (1)$$

where $P_n(s)$ is the nominal plant model, and k_t is the torque constant. $J_n = J_M + J_L$ is the nominal inertia, J_M and J_L denote the motor inertia and the load inertia, respectively. $\Delta(s) = \Delta_{\mathrm{r}}(s)\Delta_{\mathrm{high}}(s)\Delta_{\mathrm{var}}(s)$ is the unmodeled higher-order dynamics. J is the inertia, B is the damping coefficient, and K is the spring constant. The subscripts n,i and d,i represent the i-th parameters of the numerator and denominator, respectively. are the i-th inertia of the numerator and the i-th inertia of the denominator, respectively.

At first, the external disturbances in the low-frequency range under 100 Hz can arise because of changes in physical components, such as the influence of surrounding devices, mechanical wear and deformation. The external disturbances can distort control inputs or increase the time required for the system to converge to the desired state. It can be compensated using integral control methods (e.g., proportional-integral (PI) controller) or the DOB. The integral term of the PI controller adjusts the control input magnitude in proportion to the accumulated error, which allows it to compensate for errors caused by disturbance. The DOB estimates disturbances based on control input and feedback signal, which modifies control input to compensate for the disturbance.

Secondly, high-frequency noise that typically occurs in a frequency range above 1,000 Hz can result from processes

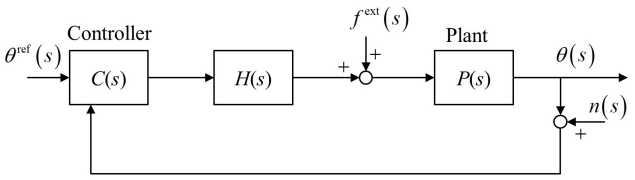

FIGURE 1. Block diagram of control system with resonance models.

such as quantization error or sensor noise. High-frequency noise can reduce the accuracy of feedback signals used in control, which makes control challenging and potentially causes sensor or actuator overloads that lead to malfunctions. High-frequency noise is typically addressed using LPF.

The unmodelled higher-order dynamics can be further divided into three categories: $\Delta_{\mathrm{r}}(s)$, $\Delta_{\mathrm{high}}(s)$ and $\Delta_{\mathrm{var}}(s)$. $\Delta_{\mathrm{r}}(s)$ represents dynamics that are unmodeled but have negligible impact on control performance and can be ignored. $\Delta_{\mathrm{high}}(s)$ describes resonance models with relatively consistent characteristics that do not significantly vary with the mover position, as found in systems such as a ball-screw system characterized by a relatively high-stiffness shaft. These resonance models typically cause resonances in the frequency range of 500 Hz to 1,000 Hz. $\Delta_{\mathrm{high}}(s)$ can be easily compensated by designing an NF as $\Delta_{\mathrm{high}}^{-1}(s)$. The ANF-based resonance suppression methods allow for setting the NF close to $\Delta_{\mathrm{high}}^{-1}(s)$ by estimating the resonance frequency of $\Delta_{\mathrm{high}}(s)$ [10], [12]. Lastly, $\Delta_{\mathrm{var}}(s)$ describes modeling errors including parametric uncertainty, and resonance models with mover-position-dependent resonance characteristics: PO. The modeling errors can be compensated for by utilizing control methods such as robust control, adaptive control and feedback control. The PO can be found in systems like a belt-drive system characterized by a belt pulley where the physical properties such as spring constant and damping coefficient vary substantially with the mover position. The PO usually triggers mid-frequency range resonances between 100 Hz and 500 Hz. $\Delta_{\mathrm{var}}(s)$ can be compensated using multiple NFs in the frequency ranges where the resonance is estimated to occur. However, using multiple NFs can decrease the stability of the system since an NF induces a phase lag in the frequency range lower than the notch frequency. Moreover, even after setting NFs, other resonances may occur when the operating range of the mover changes or the controller gains are adjusted. This resonance is difficult to suppress and may exhibit residual resonance even after an NF is configured.

III. PROPOSED RESONANCE SUPPRESSION METHOD

A. DECOUPLED PERSISTENT OSCILLATION COMPENSATOR

Figure 2 shows the block diagram of the control system using the DPOC. As shown in Fig.2, DPOC is decoupled from the controller, which allows separate design considerations. The control system in Fig.2 assumes that the controller

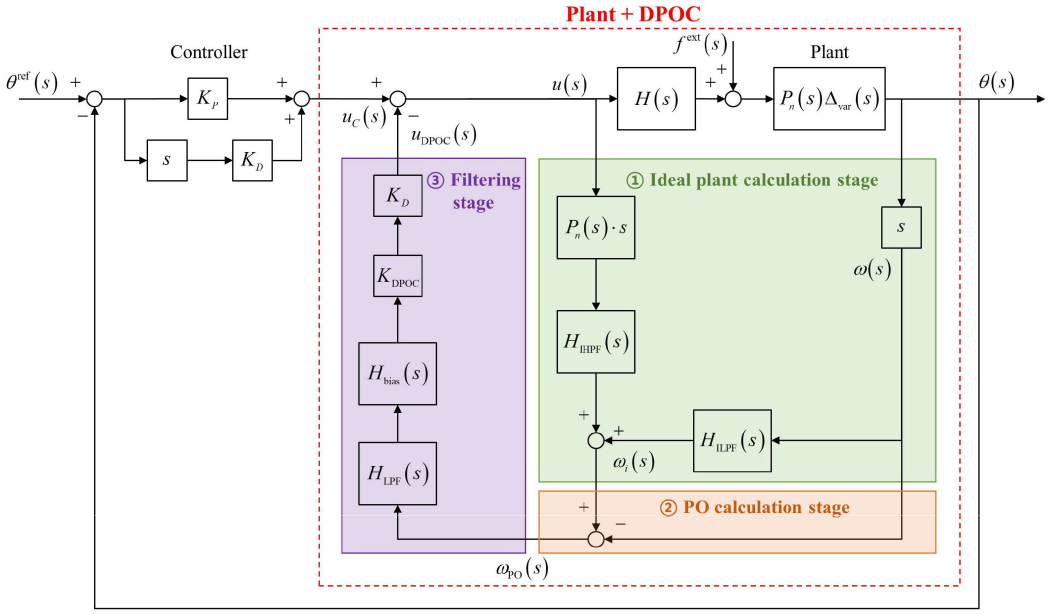

FIGURE 2. Block diagram of control system using DPOC.

is a proportional-derivative (PD) controller, and $\Delta_{\text{high}}(s)$ is canceled by NFs. The DPOC consists of three main stages to compensate for PO in the system: the ideal plant output calculation stage, the PO calculation stage and the filtering stage. In Fig.2, K_P and K_D are the proportional gain and the derivative gain of the PD controller, respectively. $u_C(s)$ is the output of the controller, $u_{\text{DPOC}}(s)$ is the output of the DPOC, and $u(s)$ is the control input to the plant. $\omega(s)$ is the measured velocity, $\omega_i(s)$ is the ideal plant output, and $\omega_{\text{PO}}(s)$ is the calculated PO which includes velocity error signals across the entire frequency range. $H_{\text{IHPF}}(s)$ and $H_{\text{ILPF}}(s)$ are the high-pass filter (HPF) and the LPF in the ideal plant output calculation stage, respectively. $H_{\text{bias}}(s)$ is the HPF to remove bias in the calculated PO. $H_{\text{LPF}}(s)$ is the LPF in the filtering stage. K_{DPOC} is the gain of the DPOC.

In the ideal plant output calculation stage, the plant velocity under ideal conditions without resonance is calculated. The resonance component in the velocity feedback is removed by filtering through the $H_{\text{ILPF}}(s)$. The velocity of the nominal plant operating based on the current command is calculated by filtering through the $H_{\text{IHPF}}(s)$. The cutoff frequencies of the $H_{\text{ILPF}}(s)$ and the $H_{\text{IHPF}}(s)$ are the same. Next, these two velocity values are added to calculate the velocity when the ideal plant operates without resonance. The ideal plant output is expressed by the following equation:

$$\begin{aligned}\omega_i(s) &= H_{\text{ILPF}}(s)\cdot\omega + H_{\text{IHPF}}(s)\cdot P_n(s)\cdot s\cdot u(s)\\ &= \frac{\omega_C}{s+\omega_C}\omega(s) + \frac{s}{s+\omega_C}\cdot\frac{k_t}{J_n s}\cdot u(s),\end{aligned} \tag{2}$$

where $f_C = \omega_C/(2\pi)$ is the cutoff frequencies of the H_{ILPF}(s) and the H_{IHPF}(s). The continuous-time domain expression of (2) is expressed as follows:

$$\dot{\omega}_i(t) = \frac{k_t}{J}\cdot u(t) + \omega_C(\omega(t) - \omega_i(t)), \tag{3}$$

which is the same as the typical state observer.

Secondly, ω_{PO}(s) is computed in the PO calculation stage by taking the difference between the ideal plant output and the measured velocity.

$$\omega_{\text{PO}}(s) = \omega_i(s) - \omega(s), \tag{4}$$

Equation (4) implies that $\omega_{\text{PO}}(s)$ converges to zero under ideal conditions when resonance does not occur.

Finally, in the filtering stage, $\omega_{\text{PO}}(s)$ within specific frequency ranges is extracted and fed back to the control system in the current unit. With this configuration, it is intuitively evident that the resonance components in a specific frequency range can be attenuated by subtracting $u_{\text{DPOC}}(s)$ from $u_C(s)$.

Applying loop transformation to the block diagram of Fig.2 as in Fig.3 allows for the analysis of how the measured velocity and the velocity when the nominal plant operates, denoted as $P_n(s).s.u(s)$, are utilized in the control system. $H_{\text{DPOC}}(s)$ in Fig.3 is $K_{\text{DPOC}}\cdot H_{\text{bias}}(s)\cdot H_{\text{LPF}}(s)\cdot H_{\text{IHPF}}(s)$. When the DPOC is used, $u(s)$ can be expressed as (5), shown at the bottom of the next page. Equation 5 means that the velocity feedback signal utilized in the controller is modified from $\omega(s)$ to $(1 - H_{\text{DPOC}}(s))\cdot\omega(s) + H_{\text{DPOC}}(s)\cdot k_t/(J_n.s)\cdot\omega(s)$ when the DPOC is applied. The measured velocity passes through $(1 - H_{\text{DPOC}}(s))$, and designing $(1 - H_{\text{DPOC}}(s))$ with a magnitude less than 0 dB allows for the attenuation of the measured velocity in a specific frequency range. The velocity signal in the frequency range with the reduced magnitude is corrected to match the velocity when the system operates as a nominal plant model. Therefore, the DPOC can compensate

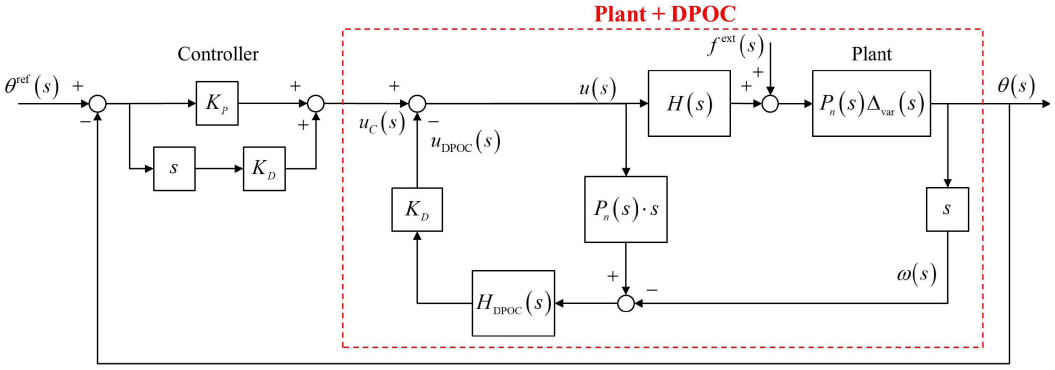

FIGURE 3. Equivalent block diagram of control system using DPOC.

for the PO by attenuating the velocity signal within a specific frequency range. Note that conventional compensators such as lag-lead compensators can be designed to respond to vibrations, but this approach is ad hoc. In contrast, the DPOC represents a structured compensation strategy that utilizes feedback signals to selectively attenuate the velocity signal within a specific frequency band, offering more targeted and effective suppression of vibrations compared to traditional compensation methods.

B. DPOC DESIGN METHOD

Consider the following system model in the continuous-time domain with a matched disturbance:

$$\dot{\mathbf{x}}(t) = \mathbf{A}\mathbf{x}(t) + \mathbf{B}u(t) + \mathbf{B}f(t), \tag{6}$$

where $\mathbf{x}(t) = [\theta(t)\ \omega(t)]^{\mathrm{T}}$ is the state vector, $\mathbf{A} = [0\ 1;0\ 0]$ is the system matrix, $\mathbf{B} = [0\ k_t/J_n)]^{\mathrm{T}}$ is the input matrix, and $f(t)$ is the matched disturbance. The matched disturbance contains unknown nonlinear terms such as parametric uncertainties, unmodeled dynamics and external disturbances. Using (3), (4) is expressed in the continuous-time domain as follows:

$$\begin{aligned}
&\dot{\omega}_{\mathrm{PO}}(t) \\
&= \dot{\omega}_i(t) - \dot{\omega}(t) \\
&= \left(\frac{k_t}{J_n}\cdot u(t) + \omega_C(\omega(t) - \omega_i(t))\right) - \frac{k_t}{J_n}\cdot(u(t) + f(t)) \\
&= -\omega_C(\omega_i(t) - \omega(t)) - \frac{k_t}{J_n}\cdot f(t).
\end{aligned} \tag{7}$$

In the presence of a matched disturbance, $\omega_{\mathrm{PO}}(s)$ does not converge to zero even when the resonance does not occur. In this case, the matched disturbance included in the output of the DPOC may hinder the proper attenuation of the measured velocity. Therefore, the filtering stage of the DPOC should include an HPF to eliminate the bias, $H_{\mathrm{bias}}(s)$, to ensure the proper functioning of the DPOC. (s) is the HPF to remove bias in the calculated PO. $H_{\mathrm{LPF}}(s)$ is the LPF in the filtering stage. K_{DPOC} is the gain of the DPOC.

When applying the DPOC, the measured velocity passes through $(1 - H_{\mathrm{DPOC}}(s))$, so the frequency characteristics of $(1 - H_{\mathrm{DPOC}}(s))$ determine the frequency band and the amount of which the magnitude of the measured velocity is attenuated. To attenuate only specific frequency bands in the measured velocity, $(1 - H_{\mathrm{DPOC}}(s))$ should have frequency characteristics similar to an NF. In this case, the measured velocity can be attenuated in the stopband of $(1 - H_{\mathrm{DPOC}}(s))$. Especially, setting the parameters of $(1 - H_{\mathrm{DPOC}}(s))$ so that its stopband includes the resonant peak frequencies of the $\Delta_{\mathrm{var}}(s)$ can enhance the effectiveness of the DPOC by increasing system damping.

$H_{\mathrm{bias}}(s)$, dedicated solely to bias removal, is set with a low cutoff frequency to minimize its impact on the frequency characteristics of $(1 - H_{\mathrm{DPOC}}(s))$. Instead, $H_{\mathrm{bias}}(s)$ is designed as a 2nd-order Butterworth HPF to effectively eliminate the influence of bias. $H_{\mathrm{LPF}}(s)$ is designed as a first-order LPF to match the order of $H_{\mathrm{IHPF}}(s)$. In this case, the cutoff frequency of $H_{\mathrm{IHPF}}(s)$ needs to be lower than that of $H_{\mathrm{LPF}}(s)$ for $(1 - H_{\mathrm{DPOC}}(s))$ to exhibit frequency characteristics similar to an NF. Thus, in the frequency range from the cutoff frequency of $H_{\mathrm{IHPF}}(s)$ to that of $H_{\mathrm{LPF}}(s)$, the DPOC can attenuate the magnitude of the measured velocity signal. This frequency band is called the 'DPOC band' in this paper. In summary,

$$\begin{aligned}
u(s) &= u_C(s) - u_{\mathrm{DPOC}}(s) \\
&= (K_P + K_D s)\cdot\left(\theta^{\mathrm{ref}}(s) - \theta(s)\right) - [K_D\cdot H_{\mathrm{DPOC}}(s)\cdot(P_n(s)\cdot s\cdot u(s) - \omega(s))] \\
&= K_P\cdot\left(\theta^{\mathrm{ref}}(s) - \theta(s)\right) + K_D\cdot\left[\omega^{\mathrm{ref}}(s) - \left\{(1 - H_{\mathrm{DPOC}}(s))\cdot\omega(s) + H_{\mathrm{DPOC}}(s)\cdot\frac{k_t}{J_n s}\cdot u(s)\right\}\right]
\end{aligned} \tag{5}$$

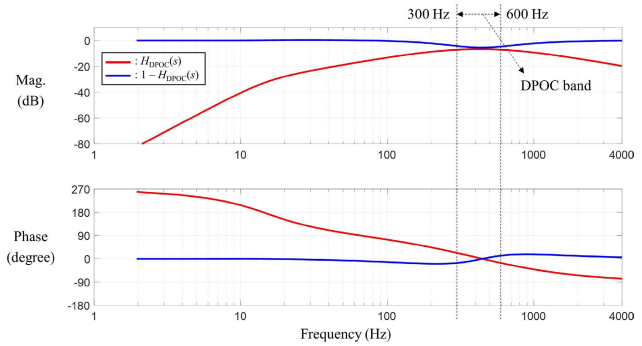

FIGURE 4. Bode plots of $H_{\mathrm{DPOC}}(s)$ and $(1 - H_{\mathrm{DPOC}}(s))$.

the transfer function of $H_{\mathrm{DPOC}}(s)$ is expressed as follows:

$$\begin{aligned} &H_{\mathrm{DPOC}}(s) \\ &= K_{\mathrm{DPOC}} \cdot H_{\mathrm{bias}}(s) \cdot H_{\mathrm{LPF}}(s) \cdot H_{\mathrm{IHPF}}(s) \\ &= K_{\mathrm{DPOC}} \cdot \frac{s^2}{s^2 + \sqrt{2}\omega_{\mathrm{bias}} s + \omega_{\mathrm{bias}}^2} \cdot \frac{\omega_L}{s + \omega_L} \cdot \frac{s}{s + \omega_H}, \end{aligned} \quad (8)$$

where $f_{\mathrm{bias}} = \omega_{\mathrm{bias}}/(2\pi)$ is the cutoff frequency of $H_{\mathrm{bias}}(s)$, $f_L = \omega_L/(2\pi)$ is the cutoff frequency of $H_{\mathrm{LPF}}(s)$, and $f_H = \omega_H/(2\pi)$ is the cutoff frequency of the $H_{\mathrm{IHPF}}(s)$. Figure 4 shows the Bode plots of $H_{\mathrm{DPOC}}(s)$ and $(1 - H_{\mathrm{DPOC}}(s))$. The parameters of the Bode plots are shown in Table 1. The Bode plot of $(1 - H_{\mathrm{DPOC}}(s))$ in Fig. 4 shows that the $(1 - H_{\mathrm{DPOC}}(s))$ can attenuate the velocity signal in specific frequency ranges including the DPOC band. Therefore, by setting the DPOC band to include the resonant peak frequencies of the mover-position-dependent resonance characteristics, the damping of the resonance characteristics is automatically modifiable. The proposed structure is designed to be linear and allows intuitive parameter setting based on frequency response, which provides tuning convenience.

Meanwhile, the DPOC gain, K_{DPOC}, determines the extent to which the magnitude of the measured velocity is reduced by DPOC. As the DPOC gain increases while keeping the remaining parameters fixed, the magnitude of $H_{\mathrm{DPOC}}(s)$ also increases, which indicates that the amount of which the measured velocity is attenuted by $(1 - H_{\mathrm{DPOC}}(s))$ becomes larger. The detailed tuning method of K_{DPOC} is covered in Section III-C.

C. COMBINED DPOC AND DOB STRUCTURE

To compensate for both PO and external disturbances, the combined DPOC and DOB structure is introduced. The control systems with the proposed method are shown in Fig. 5(a). In Fig. 5(a), the blue line represents the signal flow of the DPOC, while the red line represents the signal flow of the DOB. $Q_{\mathrm{DOB}}(s) = \omega_Q/(s + \omega_Q)$ is the Q-filter of the DOB, where $f_Q = \omega_Q/(2\pi)$ is the cutoff frequency of the Q-filter. The linear DOB is used to analyze characteristics in the frequency domain similar to DPOC and to apply the proposed method to various loads even with only a nominal plant model. The block diagram in Fig. 5(a) is equivalent to the

TABLE 1. Parameters of DPOC for simulation.

Parameters	K_{DPOC}	f_{bias}(Hz)	f_L(Hz)	f_H(Hz)
Values	0.7	15	600	300

block diagram in Fig. 5(b), which implies using $Q_{\mathrm{DOB}}(s) - Q_{\mathrm{DPOC}}(s)$ in place of the typical Q-filter in a DOB. In this paper, $Q_{\mathrm{DOB}}(s) - Q_{\mathrm{DPOC}}(s)$ is referred to as the Q-filter of the combined DPOC and DOB structure. $Q_{\mathrm{DPOC}}(s)$ is defined as

$$Q_{\mathrm{DPOC}}(s) = K_D \cdot H_{\mathrm{DPOC}}(s) \cdot P_n(s) \cdot s. \quad (9)$$

Figure 6 shows the Bode plots of $Q_{\mathrm{DOB}}(s)$, $Q_{\mathrm{DPOC}}(s)$ and $Q_{\mathrm{DOB}}(s) - Q_{\mathrm{DPOC}}(s)$ when f_Q is 48 Hz, and the parameters in Table 1 are utilized. In the frequency range near the DPOC band, $Q_{\mathrm{DOB}}(s) - Q_{\mathrm{DPOC}}(s)$ is smaller in magnitude than $Q_{\mathrm{DOB}}(s)$, which indicates that the DPOC attenuates the magnitude of the feedback signal to compensate for the PO. Note that designing the Q-filter as a second-order LPF enables the reduction of the magnitude across the entire frequency range. However, in this case, there is a risk of increased phase lag in the low-frequency range, which could lead to a degradation in control performance. Therefore, it is more advantageous for PO suppression to reduce the phase lag in the low-frequency range while decreasing the magnitude in specific frequency bands, rather than reducing the magnitude across the entire frequency range.

Assume that the position reference is zero, $H(s)$ is the bypass filter, and the plant is the same as the nominal plant. The transfer function from the external disturbance and the position feedback in the block diagram in Fig. 5(b) is given by

$$\frac{\theta(s)}{f^{\mathrm{ext}}(s)} = \frac{P_n(s)\left(1 - \left(Q_{\mathrm{DOB}}(s) - Q_{\mathrm{DPOC}}(s)\right)\right)}{\left(1 + P_n(s)\, C(s)\right)}. \quad (10)$$

When a constant external disturbance of magnitude 'a' is applied, applying the final value theorem on the transfer function (10) results in (11), as shown at the bottom of the next page. Therefore, using the DPOC and DOB together allows for compensation of both PO and external disturbances.

When $H(s)$ is the bypass filter, and there are no external disturbances, the transfer function from the output of the controller to the position feedback in the control system in Fig.5(b) is given by (12), as shown at the bottom of the next page. Figure 7 shows the poles and zeros of (12) as K_{DPOC} varies when applying the parameters from Tables 1 and 2. The arrows in Fig.7 indicate the direction in which the poles and zeros move as K_{DPOC} increases. K_{DPOC} at which the poles of (12) exist on the imaginary axis is 0.87. As K_{DPOC} increases, the poles of (12) move toward the right half plane (RHP). When K_{DPOC} is larger than 0. 87, (12) becomes unstable.

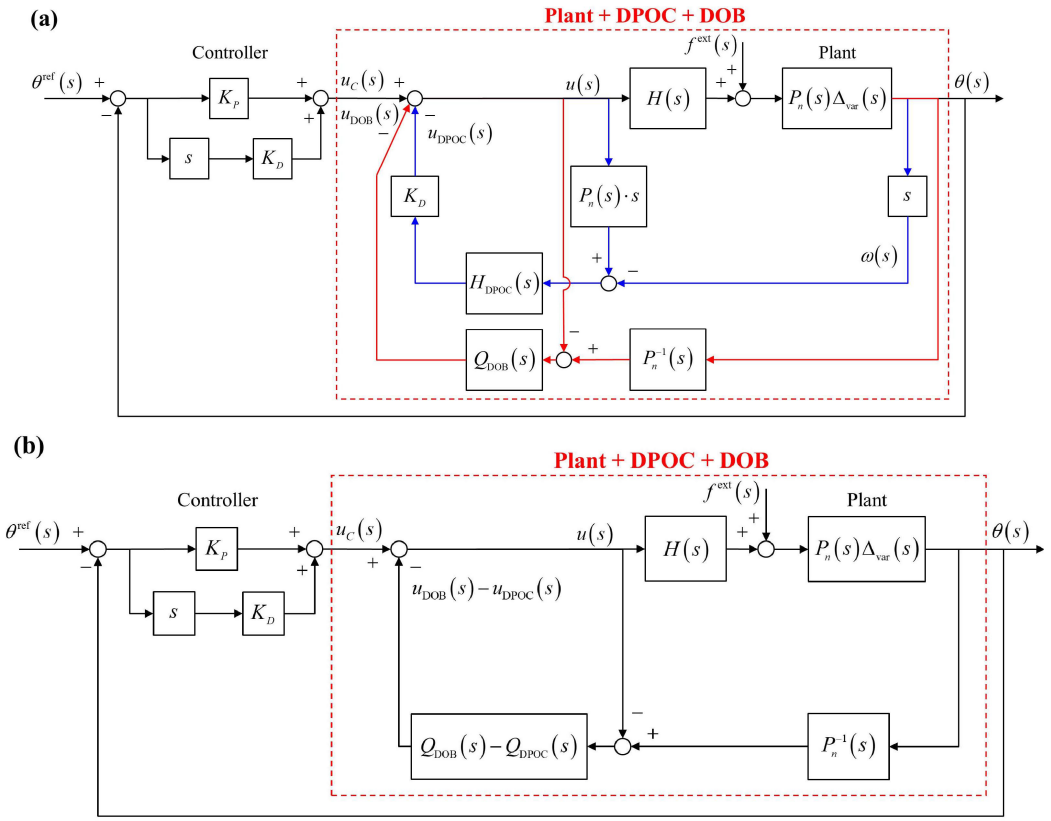

FIGURE 5. (a) Block diagrams of control system using DPOC and DOB (b) equivalent block diagram using DPOC and DOB.

Meanwhile, $Q_{\mathrm{DOB}}(s) - Q_{\mathrm{DPOC}}(s)$ is equivalent to the following transfer function.

$$Q_{\mathrm{DOB}}(s) - Q_{\mathrm{DPOC}}(s) = \frac{\omega_Q}{s+\omega_Q} - K_D \cdot \frac{k_t}{J_n s} \cdot \frac{K_{\mathrm{DPOC}}\omega_L s^3}{\left(s^2+\sqrt{2}\omega_{\mathrm{bias}}s+\omega_{\mathrm{bias}}^2\right)(s+\omega_H)(s+\omega_L)}$$

$$\begin{aligned}
\lim_{s\to 0} s\theta(s) &= \lim_{s\to 0}\left[s\cdot\frac{P_n(s)\left(1-\left(Q_{\mathrm{DOB}}(s)-Q_{\mathrm{DPOC}}(s)\right)\right)}{\left(1+P_n(s)C(s)\right)}f^{\mathrm{ext}}(s)\right] \\
&= \lim_{s\to 0}\left[s\cdot\frac{\frac{k_t}{J_n s^2}\cdot\left[1-\frac{\omega_Q}{s+\omega_Q}+K_D\cdot\frac{k_t}{J_n s}\cdot\frac{K_{\mathrm{DPOC}}\omega_L s^3}{\left(s^2+\sqrt{2}\omega_{\mathrm{bias}}s+\omega_{\mathrm{bias}}^2\right)(s+\omega_{\mathrm{VO}})(s+\omega_L)}\right]}{1+\frac{k_t}{J_n s^2}\left(K_P+K_D s\right)}\cdot\frac{a}{s}\right] \\
&= \lim_{s\to 0}\left[\frac{k_t\cdot\left[1-\frac{\omega_Q}{s+\omega_Q}+K_D\cdot\frac{k_t}{J_n s}\cdot\frac{K_{\mathrm{DPOC}}\omega_L s^3}{\left(s^2+\sqrt{2}\omega_{\mathrm{bias}}s+\omega_{\mathrm{bias}}^2\right)(s+\omega_{\mathrm{VO}})(s+\omega_L)}\right]}{J_n s^2+k_t\left(K_P+K_D s\right)}\cdot a\right]=0
\end{aligned} \tag{11}$$

$$\begin{aligned}
\frac{\theta(s)}{u_C(s)} &= \frac{P_n(s)\cdot\Delta_{\mathrm{var}}(s)}{1-\left(Q_{\mathrm{DOB}}(s)-Q_{\mathrm{DPOC}}(s)\right)+P_n(s)\cdot\Delta_{\mathrm{var}}(s)\cdot\left(Q_{\mathrm{DOB}}(s)-Q_{\mathrm{DPOC}}(s)\right)\cdot P_n^{-1}(s)} \\
&= P_n(s)\cdot\frac{\Delta_{\mathrm{var}}(s)}{1+\left(Q_{\mathrm{DOB}}(s)-Q_{\mathrm{DPOC}}(s)\right)\cdot\left[\Delta_{\mathrm{var}}(s)-1\right]}
\end{aligned} \tag{12}$$

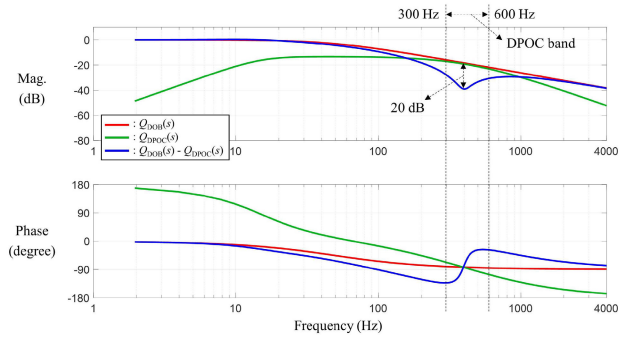

FIGURE 6. Bode plots of $Q_{DOB}(s)$, $Q_{DPOC}(s)$, and $Q_{DOB}(s)$ - $Q_{DPOC}(s)$.

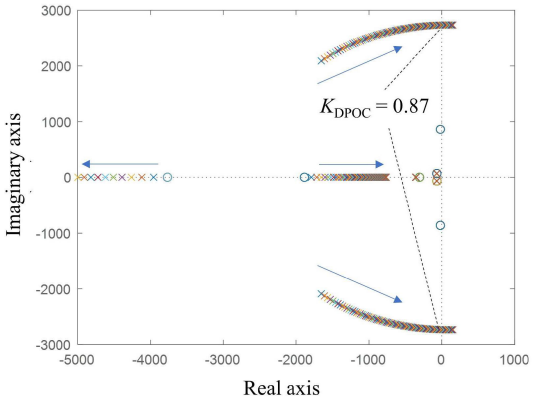

FIGURE 7. Poles and zeros of (12) for K_{DPOC} variation.

$$= \frac{\gamma_4 s^4 + (\gamma_3 - K_V K_{\text{Temp}}) s^3 + (\gamma_2 - K_V K_{\text{Temp}} \omega_Q) s^2 + \gamma_1 s + \gamma_0}{(s+\omega_Q)(s+\omega_L)(s+\omega_H)(s+\omega_{\text{bias},1})(s+\omega_{\text{bias},2})}$$
$$= \frac{b_1 s^4 + b_2 s^3 + b_3 s^2 + b_4 s + b_5}{s^5 + a_1 s^4 + a_2 s^3 + a_3 s^2 + a_4 s + a_5}, \quad (13)$$

where $K_{\text{Temp}} = k_t K_D \omega_L / J_n$, $\gamma_4 = \omega_Q$, $\gamma_3 = \omega_Q(\omega_{\text{bias}} + \omega_L + \omega_H)$, $\gamma_2 = \omega_Q(\sqrt{2}\omega_{\text{bias}}(\omega_L + \omega_H) + \omega_L\omega_H + \omega_{\text{bias}}^2)$, $\gamma_1 = \omega_Q(\sqrt{2}\,\omega_{\text{bias}}\omega_L\omega_H + \omega_{\text{bias}}^2(\omega_L + \omega_H))$, $\gamma_0 = \omega_Q\omega_L\omega_H\omega_{\text{bias}}^2$, $\omega_{\text{bias},1} = (\sqrt{2}\omega_{\text{bias}} - j\sqrt{2}\omega_{\text{bias}})/2$, and $\omega_{\text{bias},2} = (\sqrt{2}\omega_{\text{bias}} + j\sqrt{2}\omega_{\text{bias}})/2$. The transfer function (13) may exhibit RHP zeros depending on the parameter conditions. When there is an RHP zero in (13), the sign of $u_{DOB}(s) - u_{DPOC}(s)$ can change, making it difficult to predict control performance and leading to various issues such as stability degradation and increased overshoot. Therefore, it is necessary to set K_{DPOC} to avoid the occurrence of RHP zero in (13). The Routh-Hurwitz stability criterion

TABLE 2. Parameters of controller and plant for simulation.

Parameters	J_M (kg·m/s^2)	J_L (kg·m/s^2)	k_t (N·m/A)	B (N·s/m)
Values	0.27×10^{-4}	0.27×10^{-3}	0.33	0.01
Parameters	K (N/m)	K_P	K_D	
Values	200	79.33	0.53	

is used to design K_{DPOC}. The Routh-Hurwitz table of the numerator of (13) is given in (14), as shown at the bottom of the page. γ_4 and γ_0 are positive constants. Thus, all roots of the numerator of (13) are negative when C_1, C_2 and C_3 are all positive. Therefore, (13) has no RHP zero only if the following three conditions are satisfied.

$$\begin{aligned} &1) \quad \gamma_3/K_{\text{Temp}} > K_{DPOC} \\ &2) \quad \frac{(\gamma_3 - K_V K_{\text{Temp}})(\gamma_2 - K_V K_{\text{Temp}}) - \gamma_4\gamma_1}{\gamma_3 - K_V K_{\text{Temp}}} = \frac{K_1}{K_2} > 0 \\ &3) \quad \frac{K_1\gamma_1 - \gamma_0 K_2^2}{K_1} > 0 \end{aligned} \quad (15)$$

If condition 1) is satisfied, then the numerator of condition 2) can be formulated as a second-order equation for K_{DPOC} as follows:

$$\begin{aligned} &y_1(K_{DPOC}) \\ &= (\gamma_3 - K_{DPOC}K_{\text{Temp}})(\gamma_2 - K_{DPOC}K_{\text{Temp}}) - \gamma_1\gamma_4 \\ &= K_{\text{Temp}}^2 K_{DPOC}^2 - K_{\text{Temp}}(\gamma_2 + \gamma_3) K_{DPOC} + \gamma_2\gamma_3 - \gamma_1\gamma_4. \end{aligned} \quad (16)$$

Here, when $y_1(K_{DPOC})$ has two imaginary roots, $y_1(K_{DPOC})$ is always greater than zero. When $y_1(K_{DPOC})$ has a real multiple root, $y_1(K_{DPOC})$ is always greater than zero except for the real multiple root. When $y_1(K_{DPOC})$ has two real roots, denoted as $K_{DPOC,root1}$ and $K_{DPOC,root2}$ in ascending order, the conditions for $y_1(K_{DPOC})$ to be greater than zero is given by $0 < K_{DPOC} < K_{DPOC,root1}$ and $K_{DPOC,root2} < K_{DPOC}$. Using the same approach, the K_{DPOC} range under which condition 3) is always greater than 0 can be derived. If condition 2) is satisfied, then the numerator of condition 3) can be formulated as a second-order equation for K_{DPOC} as follows:

$$y_2(K_{DPOC})$$

$$\begin{array}{l|lll} s^4 & \gamma_4 & \gamma_2 - K_{DPOC}K_{\text{Temp}}\,\omega_Q & \gamma_0 \\ s^3 & \gamma_3 - K_{DPOC}K_{\text{Temp}} = C_0 & \gamma_1 & \\ s^2 & \frac{(\gamma_3 - K_{DPOC}K_{\text{Temp}})(\gamma_2 - K_{DPOC}K_{\text{Temp}}) - \gamma_4\gamma_1}{\gamma_3 - K_{DPOC}K_{\text{Temp}}} = C_1 & \gamma_0 & \\ s^1 & \frac{((\gamma_3 - K_{DPOC}K_{\text{Temp}})(\gamma_2 - K_{DPOC}K_{\text{Temp}}) - \gamma_4\gamma_1)\gamma_1 - \gamma_0(\gamma_3 - K_{DPOC}K_{\text{Temp}})^2}{(\gamma_3 - K_{DPOC}K_{\text{Temp}})(\gamma_2 - K_{DPOC}K_{\text{Temp}}) - \gamma_4\gamma_1} = C_2 & & \\ s^0 & \gamma_0 & & \end{array} \quad (14)$$

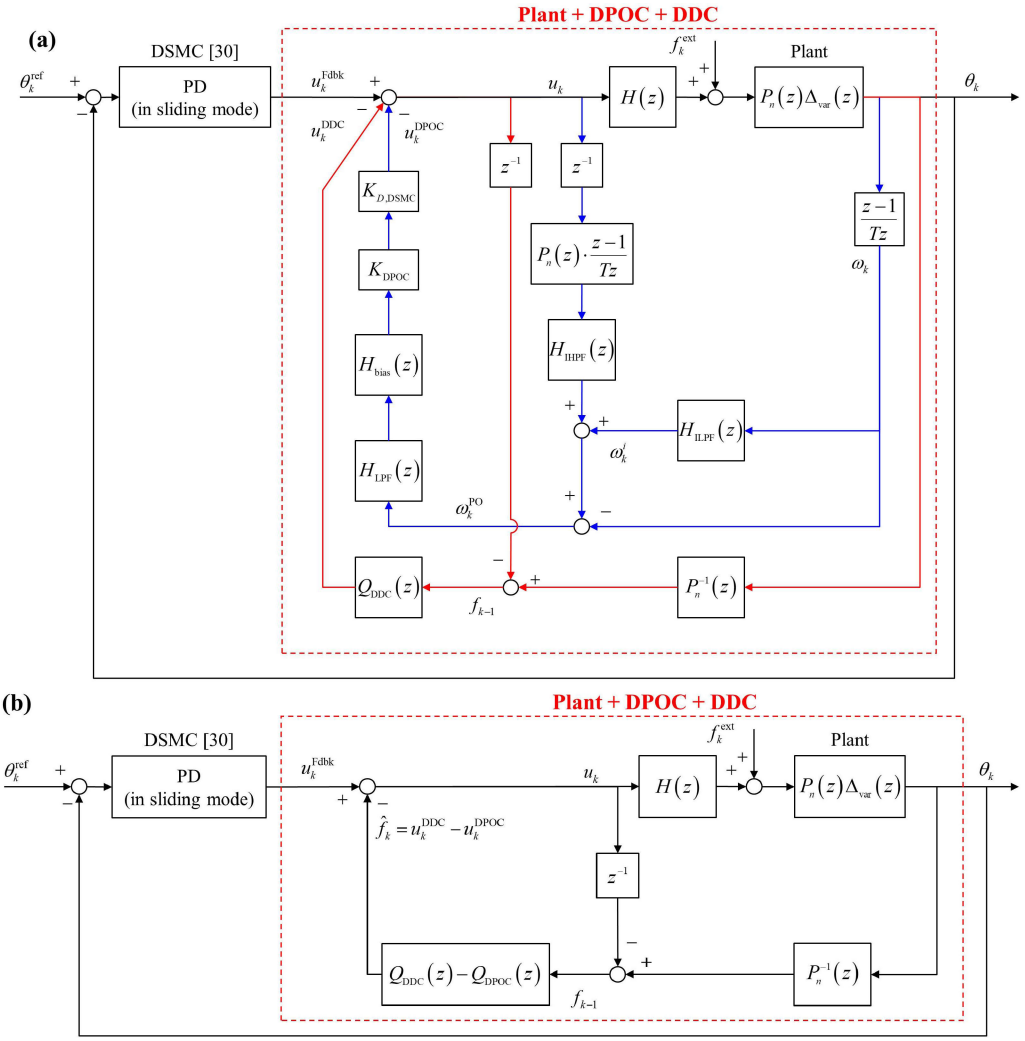

FIGURE 8. (a) Block diagram of control system using DSMC with DPOC and DDC (b) equivalent block diagram of control system using DSMC with DPOC and DDC.

$$= (\gamma_1 - \gamma_0) K_{\text{Temp}}^2 K_{\text{DPOC}}^2 - K_{\text{Temp}} (\gamma_1 (\gamma_2 + \gamma_3) - 2\gamma_0\gamma_3) K_{\text{DPOC}} + \gamma_1\gamma_2\gamma_3 - \gamma_4\gamma_1^2 - \gamma_0\gamma_3^2. \quad (17)$$

When $y_2(K_{\text{DPOC}})$ has two imaginary roots, $y_2(K_{\text{DPOC}})$ is always greater than zero. When $y_2(K_{\text{DPOC}})$ has a real multiple root, $y_2(K_{\text{DPOC}})$ is always greater than zero except for the real multiple root. When $y_2(K_{\text{DPOC}})$ has two real roots, denoted as $K_{\text{DPOC,root3}}$ and $K_{\text{DPOC,root4}}$ in ascending order, the conditions for $y_2(K_{\text{DPOC}})$ to be greater than zero is given by $0 < K_{\text{DPOC}} < K_{\text{DPOC,root3}}$ and $K_{\text{DPOC,root4}} < K_{\text{DPOC}}$. Therefore, satisfying all conditions in (15) enables the determination of the requirements for K_{DPOC} to prevent RHP zeros in (13).

IV. PROPOSED METHOD IN DISCRETE-TIME DOMAIN

A. COMBINED DPOC AND DDC STRUCTURE

In most simple loads, such as ball-screw mechanisms, PD controllers can provide excellent control performances. However, their efficacy diminishes in complex equipment and robots because of model uncertainties, external disturbances and nonlinear system behaviors. In these complex applications, using only PD controllers is insufficient, which necessitates the integration of various control strategies to enhance their effectiveness. Sliding mode control (SMC) is an excellent alternative control method that ensures state variables reach and maintain a predesigned sliding surface, even under unmodeled dynamics, external disturbances and parametric uncertainties. The SMC method can suffer from chattering because of the nonlinearity of the switching term; however, utilizing a boundary layer technique for the switching function can reduce the nonlinearity and alleviate the chattering. In the discrete-time domain, the invariant property of continuous-time SMC is lost because of the limited sampling period [30]. Instead, the state variables reach and maintain values within a specific boundary, forming a quasi-sliding mode. A discrete-time SMC (DSMC) is combined with the DDC to enable the tracking error to zero and provide robustness to unknown disturbances [30]. A recent study has researched DSMC with DDC as an equivalent structure

to DSMC with DOB in which DDC is a special type of discrete-time DOB where sliding mode dynamics and the disturbance estimation error dynamics are decoupled [31]. In this paper, the control law of DSMC with DDC method is utilized for the following reasons: i) to improve robustness to parametric uncertainties and external disturbances, and ii) to implement the proposed method in the discrete-time domain. Consider the following double integrator system in the discrete-time domain system with a matched disturbance:

$$\mathbf{x}_k = \mathbf{A}\mathbf{x}_k + \mathbf{B}u_k + \mathbf{B}f_k, \tag{18}$$

where $\mathbf{x}_k = [\theta_k \ \omega_k]^{\mathrm{T}}$ is the state vector, $\mathbf{A} = [1 \ T; \ 0 \ 1]$ is the system matrix, $\mathbf{B} = [k_t T^2/(2J_n) \ k_t T/J_n]^{\mathrm{T}}$, u_k is the input matrix, and f_k is the matched disturbance. A switching function is defined by

$$s_k = \mathbf{G}\mathbf{e}_k = \mathbf{G}\left(\mathbf{x}_k - \mathbf{x}_k^{\mathrm{ref}}\right), \tag{19}$$

where $\mathrm{G} = [g_1 \ g_2]$ is the gain vector to design the slope of the sliding manifold, $\mathrm{e}_k = \mathrm{x}_k$ - $\mathrm{x}_k^{\mathrm{ref}}$ is the error vector, and $\mathrm{x}_k^{\mathrm{ref}} = [\theta_k^{\mathrm{ref}} \ \omega_k^{\mathrm{ref}}]^{\mathrm{T}}$ is the reference vector. Then, the DSMC with DDC laws are given by:

$$u_k = -\hat{f}_k + (\mathbf{GB})^{-1}\left(\mathbf{G}\mathbf{x}_{k+1}^{\mathrm{ref}} - \mathbf{G}\mathbf{A}\mathbf{x}_k + qs_k - \eta \mathrm{sat}\left(s_k/\phi\right)\right), \tag{20}$$

$$\hat{f}_k = \hat{f}_{k-1} + g\left(\mathbf{GB}\right)^{-1}\left(s_k - qs_{k-1} + \eta \mathrm{sat}\left(s_{k-1}/\phi\right)\right), \tag{21}$$

where $\hat{f}_k$ is the estimated disturbance, q is the convergence rate of reaching phase, η is the gain of discontinuous control for disturbance rejection, 2ϕ is the thickness of the quasi-sliding mode band, and g is the gain parameter of DDC. According to [30], closed-loop sliding mode dynamics and disturbance estimation error dynamics are satisfied as follows:

$$s_{k+1} = qs_k - \eta \mathrm{sat}\left(s_k/\phi\right) + \mathbf{GB}\tilde{f}_k, \tag{22}$$

$$\tilde{f}_{k+1} = f_{k+1} - \hat{f}_{k+1} = (1-g)\tilde{f}_k + f_{k+1} - f_k, \tag{23}$$

where $\tilde{f}_k = f_k - \hat{f}_k$ is the disturbance estimation error. As evident from (22) and (23), the DDC satisfies the separation principle, where the sliding mode dynamics and disturbance estimation error dynamics are decoupled, allowing for the independent design of each. The following assumption holds for the entire paper.

Assumption 1: The changing rate of the disturbance is bounded as $|f_{k+1} - f_k| < m$, where m is a nonnegative constant. It implies that the disturbance is slowly varying.

Assumption 1 holds and parameters satisfy $0 < q < 1, 0 < g < 1, 0 < \eta/\phi < q < 1$, and $\eta > (\mathbf{GB})m/g$. Then, the absolute value of disturbance estimation error is bounded by m/g, i.e., $\left|\tilde{f}_k\right| < m/g$, and the closed-loop sliding mode dynamics are stable [30].

When the control law of DSMC is in sliding mode, $|s_k| < \phi$, it is represented as follows:

$$\begin{aligned} u_k &= -\hat{f}_k + (\mathbf{GB})^{-1}\mathbf{G}\left(\mathbf{x}_{k+1}^{\mathrm{ref}} - \mathbf{A}\mathbf{x}_k^{\mathrm{ref}}\right) \\ &\quad - (\mathbf{GB})^{-1}\mathbf{G}\left(\mathbf{A} - \left(q - \frac{\eta}{\phi}\right)\mathbf{I}_{2\times 2}\right)\mathbf{e}_k \\ &= -u_k^{\mathrm{DDC}} + u_k^{\mathrm{FF}} + u_k^{\mathrm{Fdbk}}, \\ u_k^{\mathrm{DDC}} &= \hat{f}_k, \ u_k^{\mathrm{FF}} = (\mathbf{GB})^{-1}\mathbf{G}\left(\mathbf{x}_{k+1}^{\mathrm{ref}} - \mathbf{A}\mathbf{x}_k^{\mathrm{ref}}\right), \\ u_k^{\mathrm{Fdbk}} &= -\begin{bmatrix} K_{P,\mathrm{DSMC}} & K_{D,\mathrm{DSMC}} \end{bmatrix}\mathbf{e}_k. \end{aligned} \tag{24}$$

Therefore, (20) can be decomposed into the DDC term, u_k^{DDC}, the feedforward term, u_k^{FF}, and the feedback term, u_k^{Fdbk}, within the sliding mode. In the sliding mode, the feedback term is equivalent to a PD controller, which means that the analysis content from Section III is directly applicable. The block diagrams of the control system using the DSMC with DPOC and DDC are shown in Fig. 8(a). In Fig. 8(a), the blue line represents the signal flow of the DPOC, while the red line represents the signal flow of the DDC. The feedforward term, which does not affect stability, has been omitted from the block diagram. The Q-filter of the DOB and the Q-filter of the DDC [31], $\mathrm{Q}_{\mathrm{DDC}}(\mathrm{z})$, have the following relationship.

$$\begin{aligned} &Q_{\mathrm{DDC}}(z) \\ &= Q_{\mathrm{DOB}}(s)\,|_{s=\frac{z-1}{Tz}} = \frac{\omega_Q T z}{\left(1+\omega_Q T\right)z - 1} = \frac{gz}{z-(1-g)} \end{aligned} \tag{25}$$

The block diagram in Fig. 8(a) is equivalent to the block diagram in Fig. 8(b). When the proposed method is utilized, the estimated disturbance previously calculated by DDC, u_k^{DDC}, transitions to the estimated disturbance by the proposed method, $u_k^{\mathrm{DDC}} - u_k^{\mathrm{DPOC}}$. The Q-filter of the combined DPOC and DDC structure is $Q_{\mathrm{DDC}}(\mathrm{z}) - Q_{\mathrm{DPOC}}(\mathrm{z})$. Similar to (25), $Q_{\mathrm{DPOC}}(\mathrm{z})$ is defined as

$$\begin{aligned} &Q_{\mathrm{DPOC}}(z) \\ &= K_{D,\mathrm{DSMC}} \cdot K_{\mathrm{DPOC}} \cdot H_{\mathrm{bias}}(z) \cdot H_{\mathrm{LPF}}(z) \cdot H_{\mathrm{IHPF}}(z) \\ &\quad \cdot P_n(z) \cdot \frac{z-1}{Tz} \\ &= Q_{\mathrm{DPOC}}(s)|_{s=\frac{z-1}{Tz}}. \end{aligned} \tag{26}$$

B. KEY FEATURES OF PROPOSED METHOD

In this section, it is demonstrated that the separation principle, the stability of sliding mode dynamics and the robust stability to disturbance of DSMC with DDC method in [30] are all maintained even when using the proposed method in the discrete-time domain. Using (13), the Q-filter of the combined DPOC and DDC structure can be organized as (27), shown at the bottom of the next page. The poles of (27) are defined as $\lambda_1 = 1$ - $\omega_Q T/(1+\omega_Q T)$, $\lambda_2 = 1 - \omega_L T/(1+\omega_L T)$, $\lambda_3 = 1 - \omega_H T/(1+\omega_H T)$, $\lambda_4 = 1 - \omega_{\mathrm{bias},1} T/(1+\omega_{\mathrm{bias},1} T)$, and $\lambda_5 = 1 - \omega_{\mathrm{bias},2} T/(1+\omega_{\mathrm{bias},2} T)$. (27) can also organized as (28), shown at the bottom of the next page.

Using (22) and (28), the estimated disturbance can be expressed in the discrete-time domain as

$$\begin{aligned}\hat{f}_k &= p_1\hat{f}_{k-1} - p_2\hat{f}_{k-2} + p_3\hat{f}_{k-3} - p_4\hat{f}_{k-4} + p_5\hat{f}_{k-5} \\ &\quad + q_1 f_{k-1} - q_2 f_{k-2} + q_3 f_{k-3} - q_4 f_{k-4} + q_5 f_{k-5} \\ &= p_1\hat{f}_{k-1} - p_2\hat{f}_{k-2} + p_3\hat{f}_{k-3} - p_4\hat{f}_{k-4} + p_5\hat{f}_{k-5} \\ &\quad + q_1\left(\tilde{f}_{k-1} + \hat{f}_{k-1}\right) - q_2\left(\tilde{f}_{k-2} + \hat{f}_{k-2}\right) \\ &\quad + q_3\left(\tilde{f}_{k-3} + \hat{f}_{k-3}\right) \\ &\quad - q_4\left(\tilde{f}_{k-4} + \hat{f}_{k-4}\right) + q_5\left(\tilde{f}_{k-5} + \hat{f}_{k-5}\right) \\ &= (p_1+q_1)\hat{f}_{k-1} - (p_2+q_2)\hat{f}_{k-2} + (p_3+q_3)\hat{f}_{k-3} \\ &\quad - (p_4+q_4)\hat{f}_{k-4} + (p_5+q_5)\hat{f}_{k-5} \\ &\quad + q_1\tilde{f}_{k-1} - q_2\tilde{f}_{k-2} + q_3\tilde{f}_{k-3} - q_4\tilde{f}_{k-4} + q_5\tilde{f}_{k-5} \end{aligned} \tag{29}$$

Theorem 1: Separation Principle: For the system (18), choosing the control law (20) and the disturbance estimation law (29), the following closed-loop sliding mode dynamics and disturbance estimation error dynamics are

$$s_{k+1} = q s_k - \eta \mathrm{sat}\left(\frac{s_k}{\phi}\right) + \mathbf{GB}\tilde{f}_k, \tag{30}$$

$$\begin{aligned}\tilde{f}_{k+1} &= (f_{k+1} - f_k) \\ &\quad - ((p_2+q_2) - (p_3+q_3) + (p_4+q_4) - (p_5+q_5)) \\ &\quad \times (f_k - f_{k-1}) \\ &\quad + ((p_3+q_3) - (p_4+q_4) + (p_5+q_5)) \\ &\quad \times (f_{k-1} - f_{k-2}) \\ &\quad - ((p_4+q_4) - (p_5+q_5))\,(f_{k-2} - f_{k-3}) \\ &\quad + (p_5+q_5)\,(f_{k-3} - f_{k-4}) \\ &\quad + p_1\tilde{f}_k - p_2\tilde{f}_{k-1} + p_3\tilde{f}_{k-2} - p_4\tilde{f}_{k-3} + p_5\tilde{f}_{k-4}, \end{aligned} \tag{31}$$

where sliding mode dynamics and the disturbance estimation dynamics are decoupled.

Proof: Equation (30) is the same as (22), and detailed explanations can be found in [30]. Using (29) and (30), $\tilde{f}_{k+1}$ is derived as follows:

$$\begin{aligned}\tilde{f}_{k+1} &= f_{k+1} - \hat{f}_{k+1} \\ &= f_{k+1} - (p_1+q_1)f_k + (p_2+q_2)f_{k-1} \\ &\quad - (p_3+q_3)f_{k-2} + (p_4+q_4)f_{k-3} - (p_5+q_5)f_{k-4} \\ &\quad + p_1\tilde{f}_k - p_2\tilde{f}_{k-1} + p_3\tilde{f}_{k-2} - p_4\tilde{f}_{k-3} + p_5\tilde{f}_{k-4} \\ &= (f_{k+1} - f_k) \\ &\quad - ((p_2+q_2) - (p_3+q_3) + (p_4+q_4) - (p_5+q_5)) \\ &\quad \times (f_k - f_{k-1}) \\ &\quad + ((p_3+q_3) - (p_4+q_4) + (p_5+q_5))\,(f_{k-1} - f_{k-2}) \\ &\quad - ((p_4+q_4) - (p_5+q_5))\,(f_{k-2} - f_{k-3}) \\ &\quad + (p_5+q_5)\,(f_{k-3} - f_{k-4}) \\ &\quad + p_1\tilde{f}_k - p_2\tilde{f}_{k-1} + p_3\tilde{f}_{k-2} - p_4\tilde{f}_{k-3} + p_5\tilde{f}_{k-4}. \end{aligned}$$

■

When the changing rate of the disturbance is bounded, the absolute value of $\tilde{f}_k$ is also bounded as stated in Lemma 1 below.

Lemma 1: For (31), if Assumption 1 holds with $|\lambda_1| < 1$, $|\lambda_2| < 1$, $|\lambda_3| < 1$, $|\lambda_4| < 1$, and $|\lambda_5| < 1$, then there exists some k_0 such that

$$\left|\tilde{f}_k\right| < \frac{(1-(p_2+q_2)+2\,(p_3+q_3)-3\,(p_4+q_4)+4\,(p_5+q_5))}{(1-p_1+p_2-p_3+p_4-p_5)} \cdot m$$

for all $k > k_0$ regardless of $\tilde{f}_0$.

$$\begin{aligned}&\frac{U_{\mathrm{DDC}}(z) - U_{\mathrm{DPOC}}(z)}{z^{-1}F(z)} \\ &= Q_{\mathrm{DDC}}(z) - Q_{\mathrm{DPOC}}(z) = Q_{\mathrm{DOB}}(s)|_{s=\frac{z-1}{Tz}} - Q_{\mathrm{DPOC}}(s)|_{s=\frac{z-1}{Tz}} \\ &= \frac{b_1((z-1)/Tz)^4 + b_2((z-1)/Tz)^3 + b_3((z-1)/Tz)^2 + b_4((z-1)/Tz) + b_5}{((z-1)/Tz + \omega_Q)((z-1)/Tz + \omega_L)((z-1)/Tz + \omega_H)\left((z-1)/Tz + \omega_{\mathrm{bias},1}\right)\left((z-1)/Tz + \omega_{\mathrm{bias},2}\right)} \\ &= \frac{b_1 Tz(z-1)^4 + b_2 T^2 z^2 (z-1)^3 + b_3 T^3 z^3 (z-1)^2 + b_4 T^4 z^4 (z-1) + b_5 T^5 z^5}{\left((1+\omega_Q T)z - 1\right)((1+\omega_L T)z - 1)((1+\omega_H T)z - 1)\left((1+\omega_{\mathrm{bias},1}T)z - 1\right)\left((1+\omega_{\mathrm{bias},2}T)z - 1\right)} \end{aligned} \tag{27}$$

$$\begin{aligned}&\frac{U_{\mathrm{DDC}}(z) - U_{\mathrm{DPOC}}(z)}{z^{-1}F(z)} \\ &= Q_{\mathrm{DDC}}(z) - Q_{\mathrm{DPOC}}(z) = Q_{\mathrm{DOB}}(s)|_{s=\frac{z-1}{Tz}} - Q_{\mathrm{DPOC}}(s)|_{s=\frac{z-1}{Tz}} \\ &= \frac{b_1((z-1)/Tz)^4 + b_2((z-1)/Tz)^3 + b_3((z-1)/Tz)^2 + b_4((z-1)/Tz) + b_5}{((z-1)/Tz)^5 + a_1((z-1)/Tz)^4 + a_2((z-1)/Tz)^3 + a_3((z-1)/Tz)^2 + a_4((z-1)/Tz) + a_5} \\ &= \frac{b_1 Tz(z-1)^4 + b_2 T^2 z^2 (z-1)^3 + b_3 T^3 z^3 (z-1)^2 + b_4 T^4 z^4 (z-1) + b_5 T^5 z^5}{(z-1)^5 + a_1 Tz(z-1)^4 + a_2 T^2 z^2 (z-1)^3 + a_3 T^3 z^3 (z-1)^2 + a_4 T^4 z^4 (z-1) + a_5 T^5 z^5} \\ &= \frac{q_1 - q_2 z^{-1} + q_3 z^{-2} - q_4 z^3 + q_5 z^4}{1 - p_1 z^{-1} + p_2 z^{-2} - p_3 z^{-3} + p_4 z^{-4} - p_5 z^{-5}} \end{aligned} \tag{28}$$

Proof: Divide $\tilde{f}_k$ into $\tilde{f}_{1,k}+\tilde{f}_{2,k}$ with $\tilde{f}_{1,0}=0$ and $\tilde{f}_{2,0}=\tilde{f}_0$. Then, (31) can be organized as

$$\begin{aligned}
&\tilde{f}_{1,k+1}\\
&=(f_{k+1}-f_k)\\
&\quad-((p_2+q_2)-(p_3+q_3)+(p_4+q_4)-(p_5+q_5))\\
&\quad\times(f_k-f_{k-1})\\
&\quad+((p_3+q_3)-(p_4+q_4)+(p_5+q_5))\\
&\quad\times(f_{k-1}-f_{k-2})\\
&\quad-((p_4+q_4)-(p_5+q_5))(f_{k-2}-f_{k-3})\\
&\quad+(p_5+q_5)(f_{k-3}-f_{k-4})\\
&\quad+p_1\tilde{f}_{1,k}-p_2\tilde{f}_{1,k-1}+p_3\tilde{f}_{1,k-2}\\
&\quad-p_4\tilde{f}_{1,k-3}+p_5\tilde{f}_{1,k-4},
\end{aligned}\tag{32}$$

$$\tilde{f}_{2,k+1}=p_1\tilde{f}_{2,k}-p_2\tilde{f}_{2,k-1}+p_3\tilde{f}_{2,k-2}-p_4\tilde{f}_{2,k-3}+p_5\tilde{f}_{2,k-4}.\tag{33}$$

If $\left|\tilde{f}_{1,k}\right| < \frac{(1-(p_2+q_2)+2(p_3+q_3)-3(p_4+q_4)+4(p_5+q_5))}{(1-p_1+p_2-p_3+p_4-p_5)}\cdot m$, the inequality (34), as shown at the bottom of the next page, holds. Therefore, the above inequality holds for all $k>0$. Since all poles of (27) lie within the unit circle in the z-domain, $\tilde{f}_{2,k}$ remains arbitrarily small at some time k_0 regardless of $\tilde{f}_0$. ■

Therefore, $\tilde{f}_k$ asymptotically converges to zero when the disturbance is constant or slowly varying. In these conditions, s_k in (30) also asymptotically goes to zero [30]. The robust stability of the sliding mode dynamics of the DSMC with DPOC and DDC under external disturbances is presented in Theorem 2.

Theorem 2: Robust Stability to Disturbance: For the system (18), if Assumption 1 holds and the following conditions are satisfied, the switching function enters into the small region, i.e., $|s_k|<\frac{(\mathbf{GB})Lm}{1-q+(\eta/\phi)}$, where

$$L=\frac{(1-(p_2+q_2)+2(p_3+q_3)-3(p_4+q_4)+4(p_5+q_5))}{(1-p_1+p_2-p_3+p_4-p_5)}$$

and $\frac{(\mathbf{GB})Lm}{1-q+(\eta/\phi)}<\phi$. It means that the sliding mode dynamics are always guaranteed under disturbances.

Condition 1) $0<\eta/\phi<q<1$, $|\lambda_1|<1$, $|\lambda_2|<1$, $|\lambda_3|<1$, $|\lambda_4|<1$, and $|\lambda_5|<1$;

Condition 2) $(\mathbf{GB})\,Lm<\eta$.

Proof: The proof process is based on the methodologies described in [31]. The switching function can be classified into two cases: $|s_k|>\phi$ and $|s_k|\le\phi$.

Case #1. $|s_k|>\phi$

If $s_k>\phi$, the switching function is upper bounded by s'_k, whose dynamics are given by $s'_{k+1}=qs'_k-\eta+(\mathbf{GB})\,Lm$. When the initial value of the switching function s'_k is equal to s'_0, the switching function can be represented by the following sequence:

$$s'_k=q^k\left(s'_0-\frac{(\mathbf{GB})\,Lm-\eta}{1-q}\right)+\frac{(\mathbf{GB})\,Lm-\eta}{1-q}.\tag{35}$$

s'_k converges to $((\mathbf{GB})\,Lm-\eta)/(1-q)$, which is less than zero from Assumption 1, Condition 1) and 2). Therefore, s'_k eventually enters in $|s_k|<\phi$. In the same way, s_k enters $|s_k|<\phi$ when $s_k<-\phi$.

Case #2. $|s_k|\le\phi$

If $|s_k|\le\phi$, then the switching function is sandwiched between the following two sequences:

$$s''_k=\left(q-\frac{\eta}{\phi}\right)^k\left(s''_0-\frac{(\mathbf{GB})\,Lm}{1-q+\eta/\phi}\right)+\frac{(\mathbf{GB})\,Lm}{1-q+\eta/\phi},\tag{36}$$

$$s'''_k=\left(q-\frac{\eta}{\phi}\right)^k\left(s'''_0-\frac{(\mathbf{GB})\,Lm}{1-q+\eta/\phi}\right)-\frac{(\mathbf{GB})\,Lm}{1-q+\eta/\phi},\tag{37}$$

where $s''_0=s'''_0=s_0$. From (36), (37), Assumption 1, Condition 1) and 2), s_k eventually enters in $|s_k|<\frac{(\mathbf{GB})Lm}{1-q+(\eta/\phi)}$. From the Condition 2), the following inequalities hold:

$$(\mathbf{GB})\,Lm<\eta<\eta+\phi\,(1-q)\,,\tag{38}$$

By dividing $1-q+\eta/\phi$, which is larger than zero, the inequality $\frac{(\mathbf{GB})Lm}{1-q+\eta/\phi}<\phi$ holds. Therefore, the sliding mode dynamics are stable under the slowly varying disturbance. ■

In summary, Theorem 1 demonstrates that the proposed method can be decoupled from the DSMC controller, as shown in the block diagram of Fig. 8(b), which enables separate design considerations. Lemma 1 demonstrates the convergence of the disturbance estimation error dynamics and the sliding mode dynamics under conditions of constant or slowly varying disturbances. Finally, Theorem 2 shows the robust stability of the DSMC method with the proposed method under external disturbances.

V. EXPERIMENTS

Experiments are performed to validate the effectiveness of the proposed method in an industrial belt-drive servo system. Figure 9 shows the experimental setup. The setup includes a 400 W AC servo motor (RS Automation, Korea), a 23-bit optical incremental encoder (RS Automation, Korea), a 400 W servo driver (RS Automation, Korea), a coupling, a mover, and a belt-drive load. The belt-drive load and the servo motor are mechanically connected by the coupling. The control block diagram for the experiments is the same as the block diagram in Fig. 8. A second-order Butterworth LPF with a cutoff frequency of 2,000 Hz is used to attenuate high-frequency noises, which is $H(z)$ in the block diagram in Fig. 8. The sampling period T is 0.125 ms, the torque constant k_t is 0.33 N·m/A, the motor inertia J_M is 0.27×10^{-4} kg·m^2, and the load inertia J_L is 2.97×10^{-4} kg·m^2. To show the resonance characteristics that continuously vary with the position of the mover, the Bode plots of the system are obtained by shifting the position of the mover to positions A, B, and C in Fig. 9. Position A is the starting point located 0.15 meters away from the pulley where the servo motor is attached. Position B is the location where the servo motor has completed 3.5 rotations

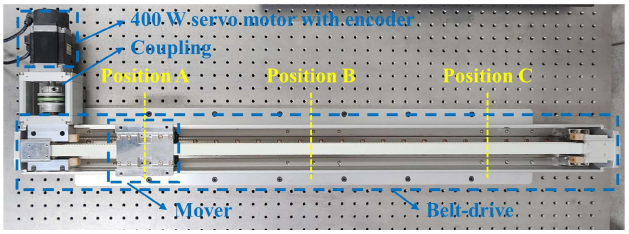

FIGURE 9. Experimental setup.

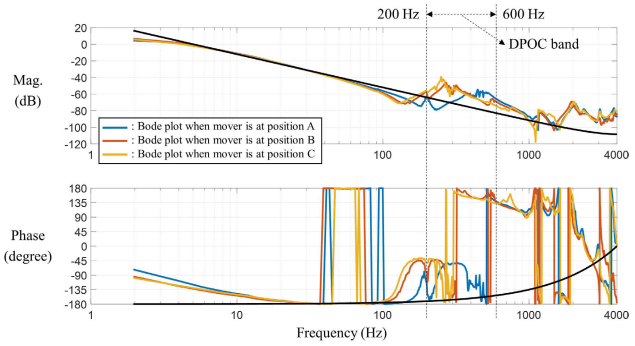

FIGURE 10. Bode plots of experimental setup with position of mover.

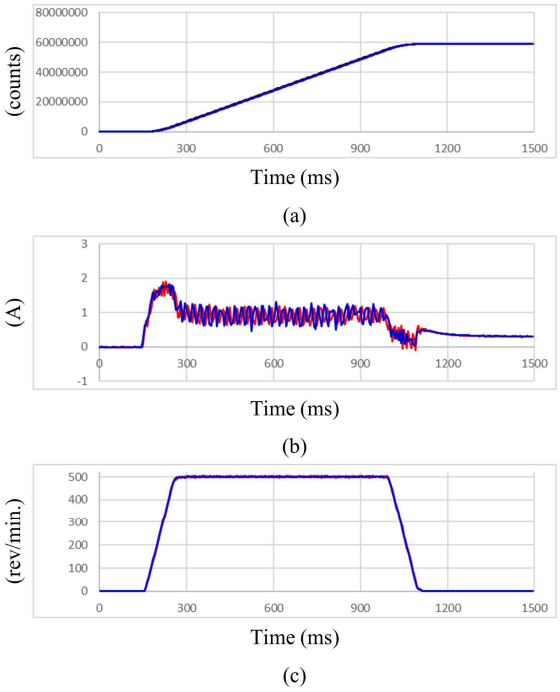

FIGURE 11. Experimental results with low gain set (black-line in (a): position reference, red-line: DSMC+DDC+ANF, blue-line: DSMC+ DPOC+DDC). (a) position data (b) current command to motor (c) velocity feedback.

from position A. Position C is the target position where the servo motor has completed 7 rotations from position A. Figure 10 shows the Bode plots of the system with the position of the mover. As shown in Fig. 10, it can be observed that the mover-position-dependent resonance characteristics where the resonant peak frequency shifts from around 500 Hz to 250 Hz as the mover moves from position A to C. The effectiveness of the proposed method is demonstrated in suppressing resonances, particularly under conditions where the PO exists in the experimental environment. The experiments that utilize DSMC with DDC and ANF method in [10] are also performed to compare the resonance suppression performance. Both methods are implemented in the servo driver. The DPOC parameters are given in Table 3. The DPOC band is set from 200 Hz to 600 Hz to cover the frequency

$$
\begin{aligned}
&- \frac{(1-(p_2+q_2)+2(p_3+q_3)-3(p_4+q_4)+4(p_5+q_5))}{(1-p_1+p_2-p_3+p_4-p_5)} \cdot m \\
&< -(1-(p_2+q_2)+2(p_3+q_3)-3(p_4+q_4)+4(p_5+q_5))\left(1+\frac{(p_1-p_2+p_3-p_4+p_5)}{(1-p_1+p_2-p_3+p_4-p_5)}\right)m \\
&= -m+((p_2+q_2)-(p_3+q_3)+(p_4+q_4)-(p_5+q_5))\,m \\
&\quad -((p_3+q_3)-(p_4+q_4)+(p_5+q_5))\,m+((p_4+q_4)-(p_5+q_5))\,m-(p_5+q_5)\,m \\
&\quad -(p_1-p_2+p_3-p_4+p_5)\frac{(1-(p_2+q_2)+2(p_3+q_3)-3(p_4+q_4)+4(p_5+q_5))}{(1-p_1+p_2-p_3+p_4-p_5)}m \\
&< \tilde{f}_{1,k+1} \\
&< m-((p_2+q_2)-(p_3+q_3)+(p_4+q_4)-(p_5+q_5))\,m \\
&\quad +((p_3+q_3)-(p_4+q_4)+(p_5+q_5))\,m-((p_4+q_4)-(p_5+q_5))\,m+(p_5+q_5)\,m \\
&\quad +(p_1-p_2+p_3-p_4+p_5)\frac{(1-(p_2+q_2)+2(p_3+q_3)-3(p_4+q_4)+4(p_5+q_5))}{(1-p_1+p_2-p_3+p_4-p_5)}m \\
&= (1-(p_2+q_2)+2(p_3+q_3)-3(p_4+q_4)+4(p_5+q_5))\left(1+\frac{(p_1-p_2+p_3-p_4+p_5)}{(1-p_1+p_2-p_3+p_4-p_5)}\right)m \\
&< \frac{(1-(p_2+q_2)+2(p_3+q_3)-3(p_4+q_4)+4(p_5+q_5))}{(1-p_1+p_2-p_3+p_4-p_5)}m
\end{aligned}
\tag{34}
$$

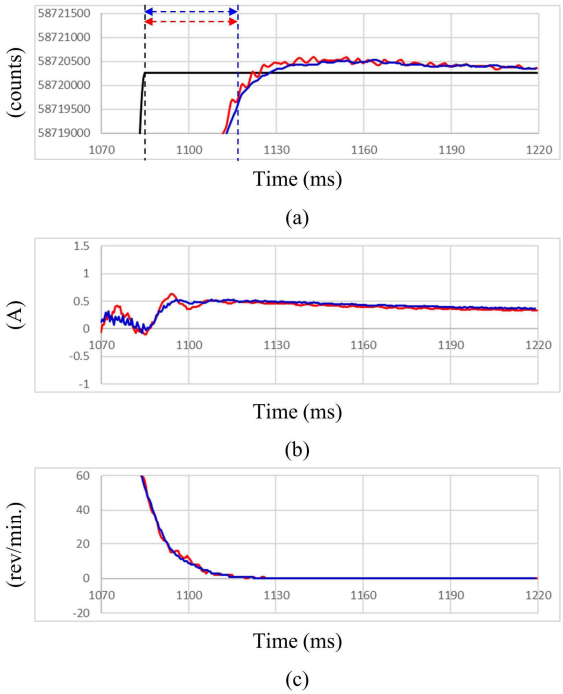

FIGURE 12. Zoomed in plot of Fig. 11 (black-line in (a): position reference, red-line: DSMC+DDC+ANF, blue-line: DSMC+DPOC+ DDC).

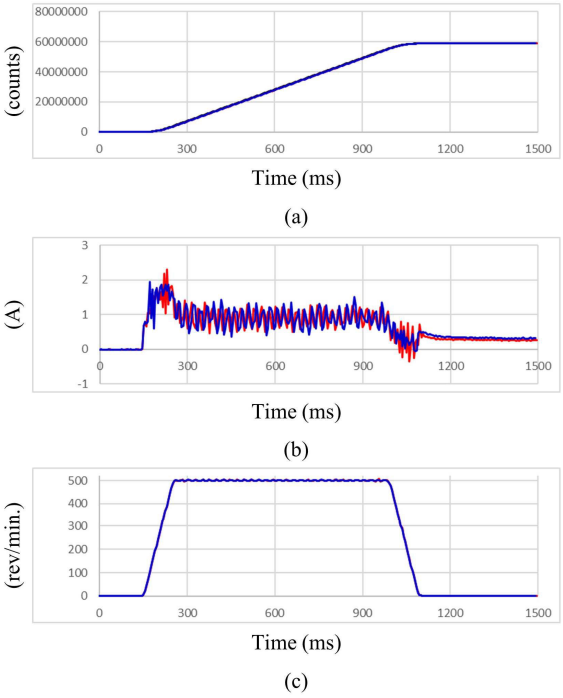

FIGURE 13. Experimental results with high gain set (black-line in (a): position reference, red-line: DSMC+DDC+ANF, blue-line: DSMC+ DPOC+DDC). (a) position data (b) current command to motor (c) velocity feedback.

ranges of resonant peak frequencies from position A to C. The gain of DPOC was set to 0.6 based on the gain boundary calculation to prevent the emergence of RHP zeros in the

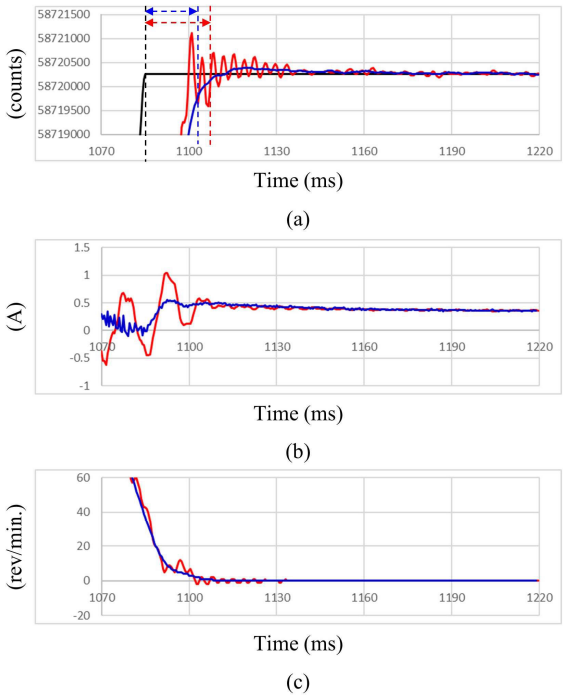

FIGURE 14. Zoomed in plot of Fig. 13 (black-line in (a): position reference, red-line: DSMC+DDC+ANF, blue-line: DSMC+DPOC+ DDC).

Q-filter of the proposed method. The transfer function of a bi-quad NFs in the experiments are given as follows:

$$H_{\mathrm{NF}}(z) = \prod_{i=1}^{4} \left. \frac{s^2 + \left(1 - k_{\mathrm{depth},i}\right) \frac{\omega_{N,i}}{Q_{N,i}} s + \omega_{N,i}}{s^2 + \frac{\omega_{N,i}}{Q_{N,i}} s + \omega_{N,i}} \right|_{s=\frac{2}{T}\cdot\frac{z-1}{z+1}}, \tag{39}$$

where $f_{N,i} = \omega_{N,i}/(2\pi)$ is the notch frequency of the i-th NF, $Q_{N,i}$ is the Q-factor of the i-th NF, and $k_{\mathrm{depth},i}$ is the depth parameter of the i-th NF. These NFs are cascaded right after the Butterworth LPF. The parameters of the NF set up using ANF are as shown in Table 4. The experiments were conducted at both low and high gain settings as shown in Table 5. By conducting experiments under various gain conditions, it is demonstrated that the proposed method effectively suppresses PO regardless of the gain condition. The overshoot and tack time are measured to compare control performances. The tack time is defined as the time difference between the end time of the position reference to the time when the position error is bounded within 500 counts. In the experiments, the desired position is 7 turns, which corresponds to $2^{23} \times 7$ counts. The desired velocity is 500 rev/min, and the acceleration and deceleration time of reference are both 100 ms.

Figure 11 illustrates the experimental results after setting the system to the low gain set in Table 5, utilizing both the DSMC with DDC and ANF method, and the DSMC with DDC and DPOC method. The zoomed-in plots around the target position for Fig. 11 are shown in Fig. 12. When applying the DSMC with DDC and ANF method, the tack time and

TABLE 3. Parameters of DPOC for experiments.

Parameters	K_{DPOC}	f_{bias}(Hz)	f_L(Hz)	f_H(Hz)
Values	0.6	15	600	200

TABLE 4. Parameters of NFs set by ANF.

Parameters	$f_{N,1}$ (Hz)	$f_{N,2}$ (Hz)	$f_{N,3}$ (Hz)	$f_{N,4}$ (Hz)
Values	254	317	600	1,813
Parameters	$Q_{N,1}$	$Q_{N,2}$	$Q_{N,3}$	$Q_{N,4}$
Values	1.27	1.13	0.92	0.707
Parameters	$k_{\mathrm{depth},1}$	$k_{\mathrm{depth},2}$	$k_{\mathrm{depth},3}$	$k_{\mathrm{depth},4}$
Values	0.70	0.72	0.91	1.00

TABLE 5. Parameter sets of controller for experiments.

Low gain set	Parameters	$\mathbf{G}$	q	η	ϕ	g
	Values	[225 1]	0.986	0.138	10	0.028
High gain set	Parameters	$\mathbf{G}$	q	η	ϕ	g
	Values	[313 1]	0.981	0.192	10	0.038

overshoot are measured at 32.5 ms and 336 counts, respectively. When applying the DSMC with DDC and DPOC method, the tack time maintains 32.5 ms, but the overshoot is reduced to 276 counts. In both cases, the system operates stably, and the tack time performances are similar; on the other hand, applying the proposed method ensures further stability and results in a lower overshoot. Figure 13 presents the experimental results after setting the system to the high gain set in Table 5 and applying both methods. Fig. 14 provides a magnified graph of the results near the target position. When applying the DSMC with DDC and ANF method, insufficient stability leads to the occurrence of resonance, causing a delayed arrival at the target position within 500 counts. The tack time is measured at 22.5 ms, and the overshoot is 860 counts. On the other hand, applying the DSMC with DDC and DPOC method ensures stability, resulting in a smooth and stable operation without resonance. The tack time is 18 ms, which is 4.5 ms faster compared to the tack time when the DSMC with DDC and ANF method is utilized. The overshoot is significantly reduced to 136 counts, which is 724 counts smaller than when using the comparative method. The experimental results demonstrate that applying the proposed method effectively compensates for the PO, allowing for stable operation without resonance.

VI. CONCLUSION

This paper introduced a novel method for suppressing mover-position-dependent resonance, overcoming the limitations of fixed-parameter filters. The DPOC effectively compensated for the mover-position-dependent resonance by attenuating the velocity signal within a specific frequency range, while the DOB effectively managed external disturbances. Utilizing the proposed method enhanced the control performances by addressing both PO and external disturbances. For discrete-time domain implementation, the DDC was utilized as an alternative to the DOB. The analyses of the robust stability of the DSMC with DPOC and DDC method were conducted. Finally, experimental results in an industrial belt-drive servo system demonstrated the effectiveness of the proposed method in PO suppression. Future work is aimed at developing a structure with similar characteristics without the need to determine the DPOC gain boundary.

REFERENCES

[1] M. F. Heertjes, H. Butler, N. J. Dirkx, S. H. van der Meulen, R. Ahlawat, K. O'Brien, J. Simonelli, K-T. Teng, and Y. Zhao, "Control of wafer scanners: Methods and developments," in *Proc. Amer. Control Conf. (ACC)*, Denver, CO, USA, Jul. 2020, pp. 3686–3703.

[2] A. H. Zamanian and E. Richer, "Adaptive notch filter for pathological tremor suppression using permanent magnet linear motor," *Mechatronics*, vol. 63, Nov. 2019, Art. no. 102273.

[3] Y. Ge, L. Yang, and X. Ma, "A harmonic compensation method for SPMSM sensorless control based on the orthogonal master-slave adaptive notch filter," *IEEE Trans. Power Electron.*, vol. 36, no. 10, pp. 11701–11711, Oct. 2021.

[4] J.-M. Yoon, W. Bahn, T.-I. Kim, J.-S. Han, S.-H. Lee, and D.-I.-D. Cho, "Discrete derivative method for adaptive notch filter-based frequency estimators," *Int. J. Control, Autom. Syst.*, vol. 15, no. 2, pp. 668–679, Mar. 2017.

[5] W. Bahn, J.-M. Yoon, N.-K. Hahm, S.-S. Lee, S.-H. Lee, and D.-I. Cho, "Application of adaptive notch filter for resonance suppression in industrial servo systems," in *Proc. 14th Int. Conf. Control, Autom. Syst. (ICCAS)*, Gyeonggi-do, South Korea, Oct. 2014, pp. 976–979.

[6] Y. Chen, M. Yang, J. Long, K. Hu, D. Xu, and F. Blaabjerg, "Analysis of oscillation frequency deviation in elastic coupling digital drive system and robust notch filter strategy," *IEEE Trans. Ind. Electron.*, vol. 66, no. 1, pp. 90–101, Jan. 2019.

[7] Y. Chen, M. Yang, Y. Sun, J. Long, D. Xu, and F. Blaabjerg, "A modified bi-quad filter tuning strategy for mechanical resonance suppression in industrial servo drive systems," *IEEE Trans. Power Electron.*, vol. 36, no. 9, pp. 10395–10408, Sep. 2021.

[8] T.-H. Oh, J.-S. Han, Y.-S. Kim, D.-Y. Yang, S.-H. Lee, and D.-I. Cho, "Deep RL based notch filter design method for complex industrial servo system," *Int. J. Control, Autom. Syst.*, vol. 18, no. 12, pp. 2983–2992, Oct. 2020.

[9] L. Hsu, R. Ortega, and G. Damm, "A globally convergent frequency estimator," *IEEE Trans. Autom. Control*, vol. 44, no. 4, pp. 698–713, Apr. 1999.

[10] W. Bahn, T.-I. Kim, S.-H. Lee, and D.-I. Cho, "Resonant frequency estimation for adaptive notch filters in industrial servo systems," *Mechatronics*, vol. 41, pp. 45–57, Feb. 2017.

[11] M. Ruderman, "One-parameter robust global frequency estimator for slowly varying amplitude and noisy oscillations," *Mech. Syst. Signal Process.*, vol. 170, May 2022, Art. no. 108756.

[12] T.-I. Kim, J.-S. Han, T.-H. Oh, Y.-S. Kim, S.-H. Lee, and D.-I. Cho, "A new accurate discretization method for high-frequency component mechatronics systems," *Mechatronics*, vol. 62, Oct. 2019, Art. no. 102250.

[13] K. Ohishi, K. Ohnishi, and K. Miyachi, "Torque-speed regulation of DC motor based on load torque estimation method," in *Proc. JIEE/Int. Power Electron. Conf.*, 1983, pp. 1209–1218.
[14] M. Matsuoka, T. Murakami, and K. Ohnishi, "Vibration suppression and disturbance rejection control of a flexible link arm," in *Proc. 21st Annu. Conf. IEEE Ind. Electron.*, Orlando, FL, USA, Nov. 1995, pp. 1260–1265.
[15] A. Hace, K. Jezernik, and A. Sabanovic, "SMC with disturbance observer for a linear belt drive," *IEEE Trans. Ind. Electron.*, vol. 54, no. 6, pp. 3402–3412, Dec. 2007.
[16] H. Kobayashi, S. Katsura, and K. Ohnishi, "An analysis of parameter variations of disturbance observer for motion control," *IEEE Trans. Ind. Electron.*, vol. 54, no. 6, pp. 3413–3421, Dec. 2007.
[17] J. S. Bang, H. Shim, S. K. Park, and J. H. Seo, "Robust tracking and vibration suppression for a two-inertia system by combining backstepping approach with disturbance observer," *IEEE Trans. Ind. Electron.*, vol. 57, no. 9, pp. 3197–3206, Sep. 2010.
[18] Z. Yu, T. Yang, Y. Ruan, T. Xu, and T. Tang, "A rate-difference disturbance observer control for a timing-belt servo system," *IEEE Trans. Ind. Electron.*, vol. 69, no. 11, pp. 11458–11467, Nov. 2022.
[19] Y. Jiang, J. Yang, and S. Li, "Multi-frequency-band uncertainties rejection control of flexible gimbal servo systems via a comprehensive disturbance observer," *IEEE Trans. Circuits Syst. I, Reg. Papers*, vol. 71, no. 2, pp. 794–804, Feb. 2024.
[20] L. Zheng, Q. Guan, X. Wang, Y. Luo, and Y. Wu, "A robust resonance suppression method for linear tooth belt drive with variable resonance frequency," *IEEE Trans. Ind. Electron.*, vol. 71, no. 9, pp. 10346–10355, Sep. 2024.
[21] Y. Yoshiura, S. Kawahara, D. Horimai, T. Asai, and Y. Kaku, "Vibration suppression control using an equivalent rigid-body observer," *IEEJ J. Ind. Appl.*, vol. 7, no. 5, pp. 396–402, Sep. 2018.
[22] Q. Xin, C. Wang, C.-Y. Chen, G. Yang, and L. Chen, "Robust vibration control based on rigid-body state observer for modular joints," *Machines*, vol. 9, no. 9, p. 194, Sep. 2021.
[23] D. Shang, X. Li, M. Yin, and F. Li, "Vibration suppression for two-inertia system with variable-length flexible load based on neural network compensation sliding mode controller and angle-independent method," *IEEE/ASME Trans. Mechatronics*, vol. 28, no. 2, pp. 848–859, Apr. 2023.
[24] C. Qian, C. Hua, L. Zhang, and Z. Bai, "Adaptive neural torsional vibration suppression of the rolling mill main drive system subject to state and input constraints with sensor errors," *J. Franklin Inst.*, vol. 357, no. 17, pp. 12886–12903, Nov. 2020.
[25] H. Chang, S. Lu, G. Huang, S. Zheng, and B. Song, "An extended active resonance suppression scheme based on a dual-layer network for high-performance double-inertia drive system," *IEEE Trans. Power Electron.*, vol. 38, no. 11, pp. 13717–13729, Nov. 2023.
[26] Y. Meng, Z. Chen, W.-W. Huang, X. Zhang, C. Hu, and L. Zhu, "An enhanced real-time iterative compensation method for fast tool servos with resonance suppression," *IEEE Trans. Ind. Electron.*, vol. 71, no. 6, pp. 6183–6192, Jun. 2024.
[27] C. Liu, W. Gao, and P. Gao, "Vibration suppression method for a two-link flexible manipulator based on adaptive iterative learning algorithm," *J. Vib. Eng. Technol.*, vol. 12, no. 1, pp. 587–599, Jan. 2023.
[28] J. Wu, J. Zhang, B. Nie, Y. Liu, and X. He, "Adaptive control of PMSM servo system for steering-by-wire system with disturbances observation," *IEEE Trans. Transport. Electrific.*, vol. 8, no. 2, pp. 2015–2028, Jun. 2022.
[29] B. Wang, M. Iwasaki, and J. Yu, "Command filtered adaptive backstepping control for dual-motor servo systems with torque disturbance and uncertainties," *IEEE Trans. Ind. Electron.*, vol. 69, no. 2, pp. 1773–1781, Feb. 2022.
[30] Y. Eun, J.-H. Kim, K. Kim, and D.-I. Cho, "Discrete-time variable structure controller with a decoupled disturbance compensator and its application to a CNC servomechanism," *IEEE Trans. Control Syst. Technol.*, vol. 7, no. 4, pp. 414–423, Jul. 1999.
[31] J.-S. Han, T.-I. Kim, T.-H. Oh, Y.-S. Kim, J.-H. Lee, S.-O. Kim, S.-S. Lee, and S.-H. Lee, "Frequency-domain design method for discrete-time sliding mode control and generalized decoupled disturbance compensator with industrial servo applications," in *Proc. IFAC Symp. Robot Control (SYROCO)*, Budapest, Hungary, 2018, pp. 96–101.

YOUNG-SEOK KIM received the B.S. degree from the Department of Electronic and Electrical Engineering, Sungkyunkwan University, Suwon, South Korea, in 2018. He is currently pursuing the Ph.D. degree with the Department of Electrical and Computer Engineering, Seoul National University, Seoul, South Korea. His research interests include applications of nonlinear control theory to servo drive and sensors for motion control applications.

TAE-HO OH received the B.S. and Ph.D. degrees in electrical and computer engineering from Seoul National University, Seoul, South Korea, in 2017 and 2023, respectively. His research interests include applications of nonlinear control theory and machine learning algorithms to servo drive and sensors.

DAE-YOUNG YANG received the B.S. degree from the Department of Electronic Engineering, Tsinghua University, Beijing, China, in 2017. He is currently pursuing the Ph.D. degree with the Department of Electrical and Computer Engineering, Seoul National University, Seoul, South Korea. His research interests include applications of power system control and nonlinear control theory to servo drive.

SANG-HOON LEE (Member, IEEE) received the B.S., M.S., and Ph.D. degrees in electrical and computer engineering from Seoul National University, Seoul, South Korea, in 1991, 1993, and 1997, respectively. He is currently the Research and Development Center Manager of RS Automation Company Ltd., Pyeongtaek, South Korea. His current research interests include nonlinear control theory and its application to electric machines and factory automation.

DONG-IL (DAN) CHO (Member, IEEE) received the Bachelor of Science degree from Carnegie Mellon University, USA, in 1980, and the Master of Science and Ph.D. degrees from Massachusetts Institute of Technology, USA, in 1984 and 1988, respectively. From 1987 to 1993, he was an Assistant Professor with the Department of Mechanical and Aerospace Engineering, Princeton University, USA. From 1993 to 2023, he was an Assistant Professor, an Associate Professor, and a Professor with the Department of Electrical and Computer Engineering, Seoul National University, South Korea. Since 2023, he has been the Chief Science Officer with RS Automation Company, South Korea. He has published over 150 journal articles and 150 patents. His research interests include the nonlinear and intelligent control of robotic and mechatronic systems, MEMS-fabrication, and sensor technologies. He served on the editorial board for many international journals, including the Co-Editor-in-Chief for *Mechatronics* (IFAC) and a Senior Editor for IEEE JOURNAL OF MICROELECTROMECHANICAL SYSTEMS. He served as the President for ICROS and a BOG Member for IEEE CSS and EDS. He is currently the President of IFAC. He was elected as an Ordinary Member (2010–2012), a Senior Member from 2013 to 2017, from 2018 to 2023, and in 2024, a Senior Fellow of the National Academy of Engineering of Korea since 2024.